

Supporting Information

Determining the Limiting Factor of the Electrochemical Stability Window for PEO-based Solid Polymer Electrolyte: Main chain or terminal –OH group?

*Xiaofei Yang,^a Ming Jiang,^b Xuejie Gao,^a Danni Bao,^c Qian Sun,^a Nathaniel Holmes,^a Hui Duan,^a Sankha Mukherjee,^b Keegan Adair,^a Changtai Zhao,^a Jianwen Liang,^a Weihai Li,^a Junjie Li,^a Yang Liu,^c Huan Huang,^c Li Zhang,^d Shigang Lu,^d Qingwen Lu,^a Ruying Li,^a Chandra Veer Singh^{*b}, and Xueliang Sun^{*a}*

^a. Department of Mechanical and Materials Engineering, University of Western Ontario, London, Ontario, N6A 5B9, Canada

^b. Department of Materials Science and Engineering, University of Toronto, Toronto, Ontario, M5S 3E4, Canada

^c. Glabat Solid-State Battery Inc., 700 Collip Circle, London, ON, N6G 4X8, Canada

^d. China Automotive Battery Research Institute, Beijing, 100088, P. R. China

Experimental Section

Synthesis of SPEs: The poly(ethylene glycol) dimethyl ether (PEGDME, $M_n=2000$), poly(ethylene glycol) distearate (PEG-distearate, $M_n=930$) and poly(ethylene glycol) (PEG, $M_n=400$, 2000 and 20000) based SPEs were prepared using a solution-free method. A mixture of PEGDME (or PEG, or PEG-distearate) and Li-salts (lithium (trifluoromethylsulfonyl) imide (LiTFSI) and/or lithium bis(fluorosulfonyl)imide (LiFSI)) was directly heated to 120 °C and held at that temperature until the polymers were completely melted and salts were entirely dissolved. A piece of Celgard 3501 separator (porosity: 55%, thickness: 25 μm) was immersed in this solution for 5-10 s until the separator was completely wetted. The excess liquid on the separator was removed and the obtained SPEs were marked as PEGDME (or PEG, or PEG-distearate)-x. x is the molar ratio of LiTFSI/LIFSI. For single LiTFSI and LiFSI salt, the x is 10 and 0, respectively. Moreover, PEG SPEs with PEG molecular weights $M_n=400$ and 20000 are labelled as PEG(400)-x SPE and

PEG(20000)-x SPE, respectively. The thicknesses of obtained PEGDME(PEG)-x SPEs are controlled as around 50 μm . All the aforementioned processes were conducted in an Ar-filled glove box.

Synthesis of LiFePO_4 (LFP) and $\text{LiNi}_{0.5}\text{Mn}_{0.3}\text{Co}_{0.2}\text{O}_2$ (NMC532) electrodes: The LFP and NMC532 electrodes were fabricated using a blade casting technique. For the LFP cathode, the LFP powders, C_{65} conductive carbon and PEO-PEGDME/LITFSI (EO/Li=12/1 and PEO (Mw:1000000)/PEGDME = 1:1) were dissolved in water with a weight ratio of 7:1:2 to form a slurry and then coated onto aluminum (Al) foil. The Al foil coated with slurry was then dried in a 60 $^{\circ}\text{C}$ oven overnight. For the NMC532 cathode, the NMC532 powders, C_{65} conductive carbon and PVDF-PEGDME/LITFSI (EO/Li=12/1 and polyvinylidene fluoride (PVDF)/PEGDME = 1:1) were dissolved in N-methyl-2-pyrrolidone (NMP) with a weight ratio of 7:1:2 to form a slurry and then coated onto aluminum (Al) foil. The Al foil coated with slurry was then dried in an 80 $^{\circ}\text{C}$ oven overnight.

Materials Characterization: The morphology of the Celgard 3501 separator and the Li anodes was examined by scanning electron microscopy (SEM, Hitachi S-4800 and Hitachi S-3400). X-ray diffraction (XRD) patterns were obtained using a Bruker AXS D8 Advance with a $\text{Cu K}\alpha$ radiation ($\lambda = 1.54178 \text{ \AA}$). Data collection was performed by scanning 1s per step with a step width of 0.02 from 10 $^{\circ}$ to 50 $^{\circ}$ (2 θ). X-ray Photoelectron Spectroscopy (XPS) was performed using Thermo Scientific K-Alpha with $\text{Al K}\alpha$ -radiation. All the Li anodes were washed with 1,2-dimethoxyethane (DME) solvent before SEM and XPS testing.

DFT calculations: All calculations were carried out within the DFT framework as implemented in Vienna *Ab Initio* Simulation Package (VASP). The projector augmented-wave pseudopotentials were used to describe the interaction between ions and electrons, and the exchange-correlation

effects were treated using the Perdew–Burke–Ernzerhof (PBE) functional under the generalized gradient approximation (GGA).¹ Herein, the electronic configurations for the PAW potentials were $1s^2 2s^1$ for Li, $2s^2 2p^4$ for O, $2s^2 2p^2$ for C, $1s^1 2p^0$ for H. The VESTA package was used to visualize the molecular and surface structures.² The schematic views of PEG, PEGDME and PEG-distearate molecules are provided in [Figure S25](#). The Li surface was generated through the cleavage of the optimized bulk crystal along low index surface orientation of (100). Then, the slabs with 5 layers containing 180 atoms for adsorbing PEG and PEGDME molecules, and 320 atoms for adsorbing PEG-distearate molecule were considered, where the two bottom layers were fixed while all other atoms could relax. The vacuum space in the z direction was about 20 Å to avoid the interactions between neighboring. The k-point mesh was set to be $4 \times 2 \times 1$ for Li slab surface containing adsorbed molecules and kinetic energy cutoff 450 eV was used. All the atoms of system were optimized until the total energies converged to below 10^{-4} eV and the forces acting on atoms were less than 10^{-3} eV/Å.

The surface energies were calculated using the following expression, $E_{\text{surf}} = (E_{\text{slab}} - nE_{\text{bulk}}) / 2S$, where E_{surf} is the surface energy, E_{slab} is the energy of the slab containing n units of Li, E_{bulk} is the bulk energy per unit, and S is the area of the slab surface. In order to improve the description of the interaction between adsorbed molecules and Li metal surfaces, the DFT-D3 method was employed, which has been demonstrated to give the best trade-off between computational cost and the correction for the adsorption energy of the adsorbed molecules.^{3, 4} Different adsorption positions for molecules, which contain bridge, top and parallel site have been explored.

The adsorption energy was determined using the expression, $E_B = E_{\text{Li/molecule}} - (E_{\text{Li}} + E_{\text{molecule}})$, where $E_{\text{Li/molecule}}$, E_{Li} and E_{molecule} represent the total energy of the Li surfaces containing the adsorbed molecules, the clean surface and the adsorbed molecules, respectively.⁵ Besides, the

electric field in VASP was realized by adding an artificial dipole sheet at the center of the PEG and PEGDME molecules. The total energy changes $\Delta E = E_{\text{Total}} - E_{\text{Applied}}$ of this configuration can be calculated depending on the intensity of the electric field, where E_{Total} and E_{Applied} are the total energy without and with electric field, respectively.

Electrochemical measurements: The electrochemical performance of Li-LFP/NMC532 batteries and Li-Li symmetrical cells was tested with CR2032 coin cells assembled in an Ar-filled glove box. The LFP/NMC cathode and Li anode were separated by the SPEs. The galvanostatic charge-discharge tests were carried out using a LAND CT-2001A system with operating voltages ranging from 2.7 to 4.0 V for the Li-LFP coin cell (2.5-4.3V or 2.5-4.5 V for Li-NMC532 coin cell). For pouch cell testing, the Li-LFP cell and Li-NMC532 cells were tested using the operating voltage windows of 2.0-3.9 V and 2.5-4.2 V, respectively. After charging at a constant current, the cells were further charged at constant voltages of 3.9 V and 4.2 V until the current dropped to 10% of the constant current value. All the charging current density was controlled as 0.1 C with different discharging current densities during pouch cell testing. Constant current densities were applied to the electrodes during the repeated Li stripping/plating process. The voltage and discharge capacities mentioned in this work correspond to Li^+/Li and active materials LFP or NMC. The 1C rate is determined to be 170 mA g^{-1} and 160 mA g^{-1} in Li-LFP and Li-NMC532 cell testing respectively.

The ionic conductivity of the electrolytes was determined by EIS measurement using stainless steel | SPE | stainless steel symmetric cells with controlled temperature. The electrochemical stability windows (ESWs) were measured using Al foil | SPE | Li metal and C65 | SPE | Li metal cells.

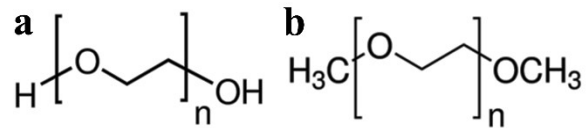


Figure S1. Molecular formulas for (a) PEG and (b) PEGDME.

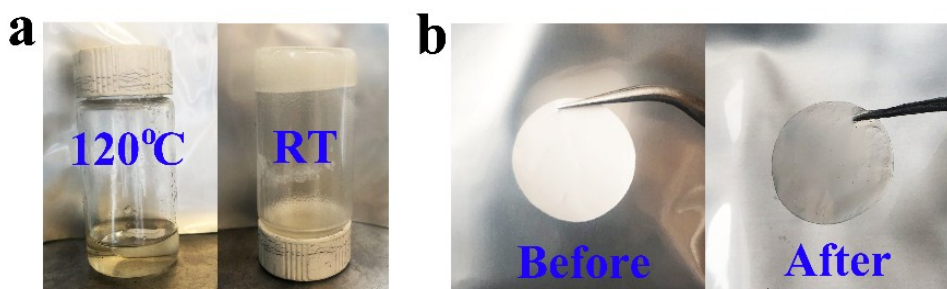


Figure S2. Optical image of (a) PEGDME with a LITFSI/LIFSI ratio of 4/1 at 120 °C and room temperature. (b) Celgard 3501 separator before and after impregnation of SPE.

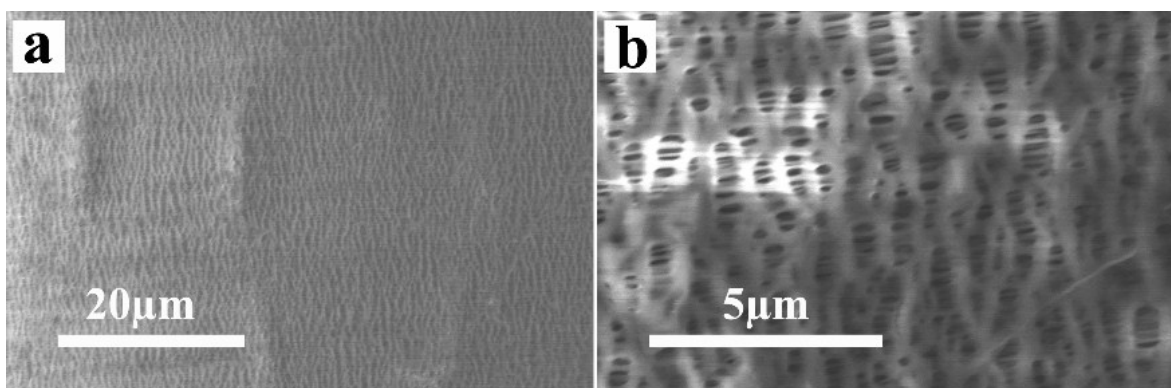


Figure S3. SEM images of Celgard 3501 at different magnifications.

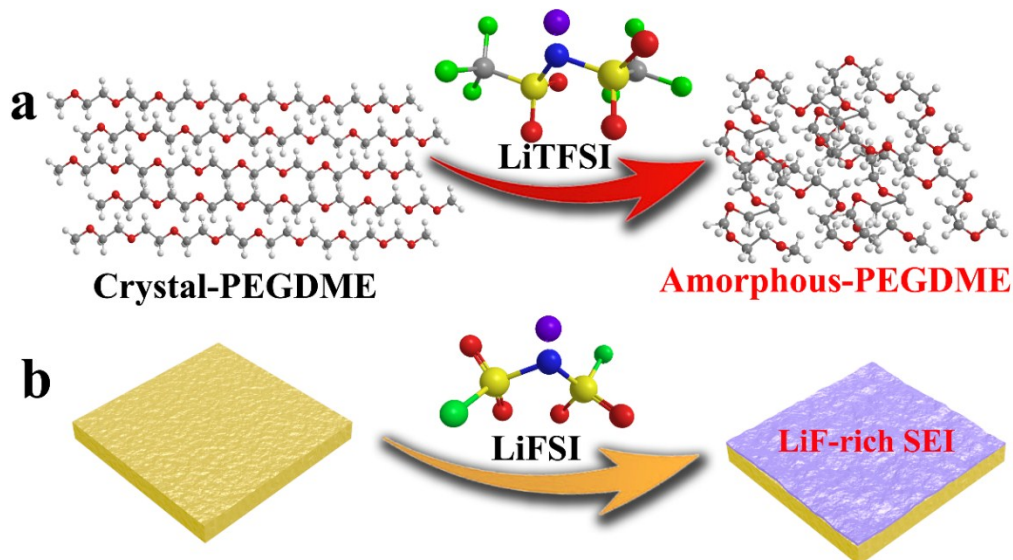


Figure S4. Functions of (a) LiTFSI and (b) LiFSI.

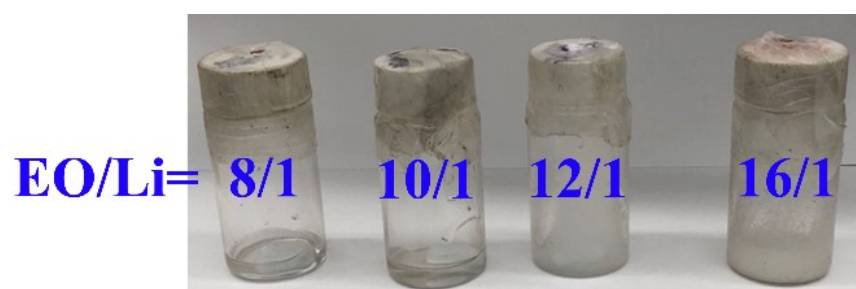


Figure S5. Optical images of the SPEs with different EO/Li ratios.

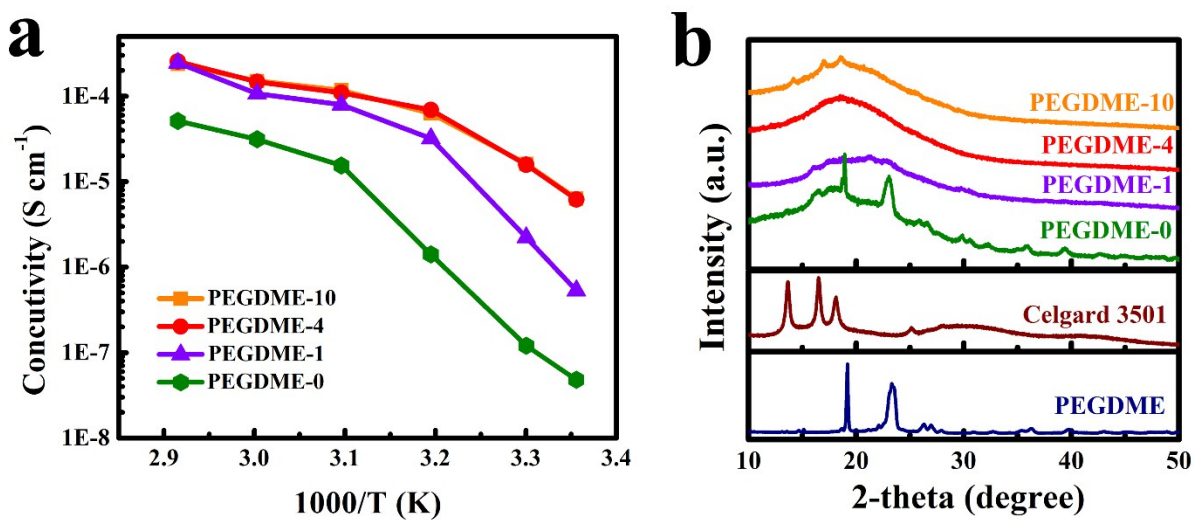


Figure S6. (a) Ionic conductivity and (b) XRD patterns of PEGDME-x SPEs.

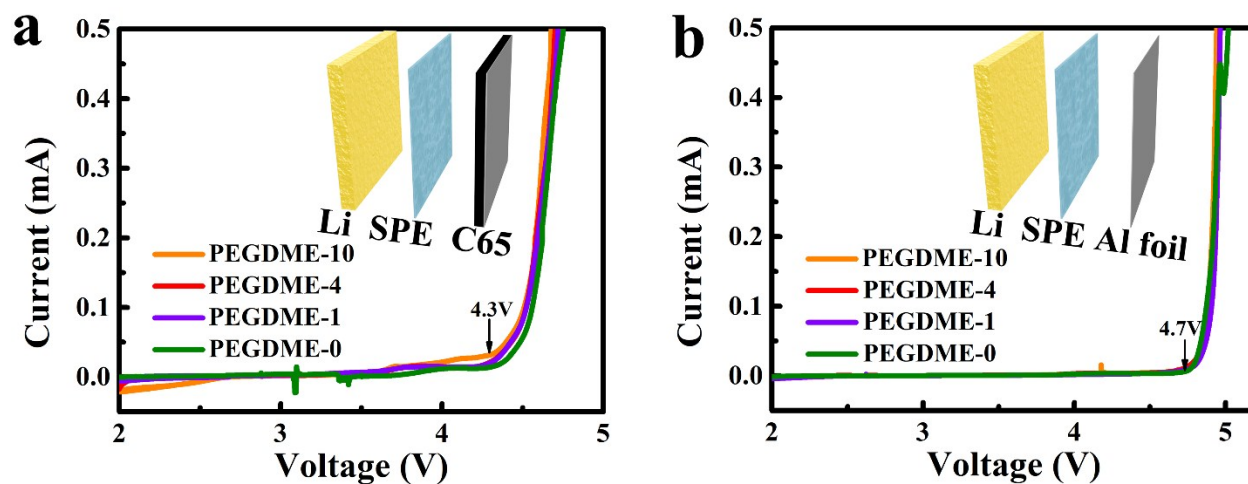


Figure S7. Electrochemical stability windows of PEGDME-x SPEs within (a) Li|SPE|C65 and (b) Li|SPE|Al foil cells.

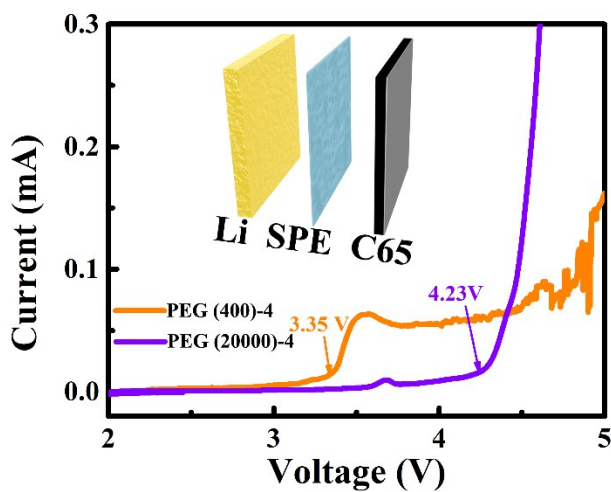


Figure S8. Electrochemical stability windows of PEG (400)-4 and PEG (20000)-4 SPEs using Li|SPE|C65 cells.

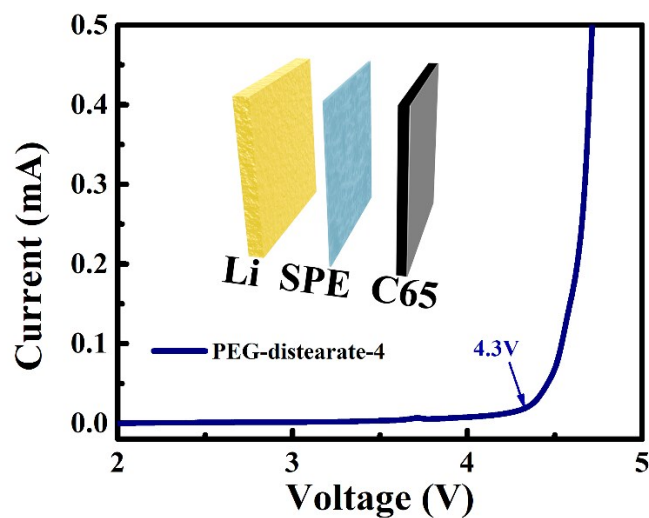


Figure S9. Electrochemical stability windows of PEG-distearate-4 SPE using Li|SPE|C65 cells.

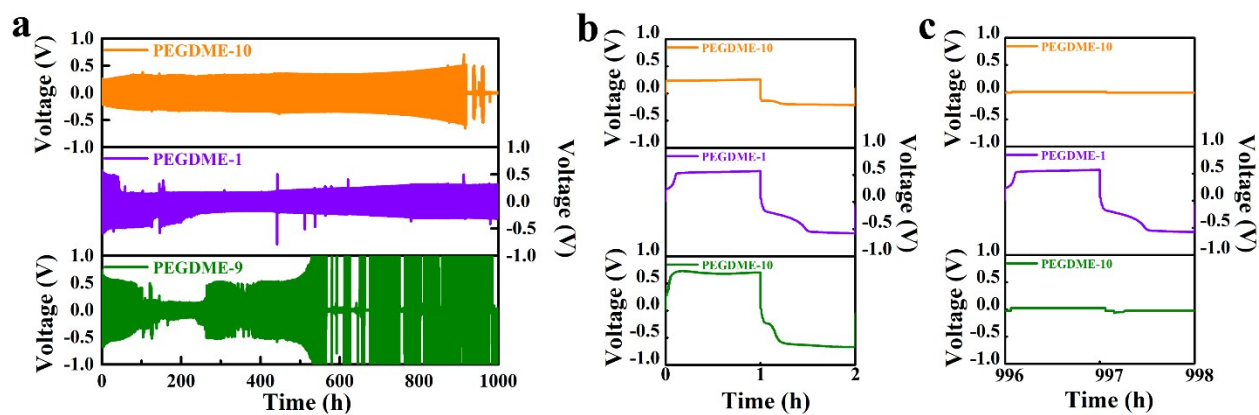


Figure S10. (a) Cycling performance of Li-Li symmetrical cells with PEGDME- x SPEs ($x=10, 1, 0$) and (b-c) plating/stripping profiles at different cycles with a current density of 0.2 mA cm^{-2} (capacity: 0.2 mAh cm^{-2}).

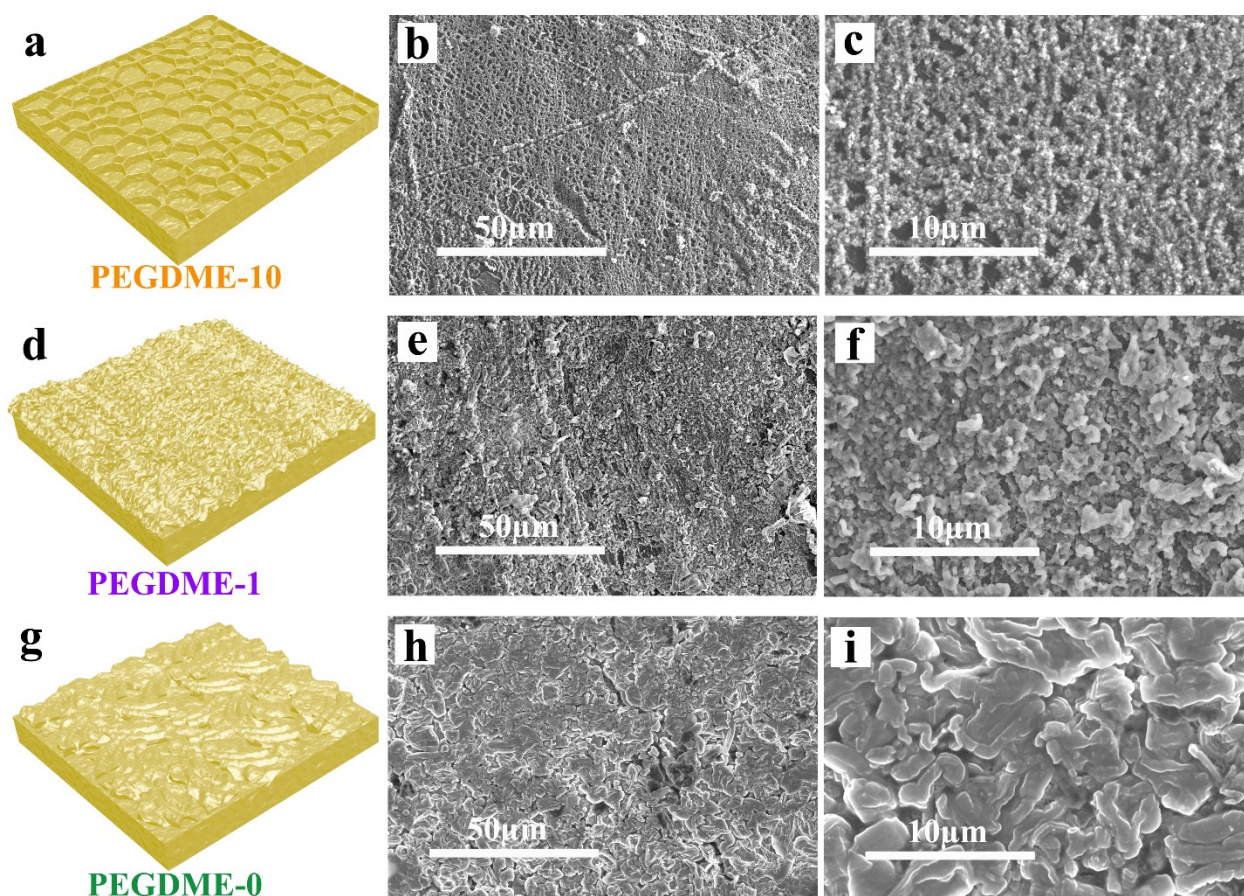


Figure S11. Schematic illustration of Li deposition morphology and SEM images of Li after 50 h of plating and stripping in (a-c) PEGDME-10, (d-f) PEGDME-4 and (g-i) PEGDME-0.

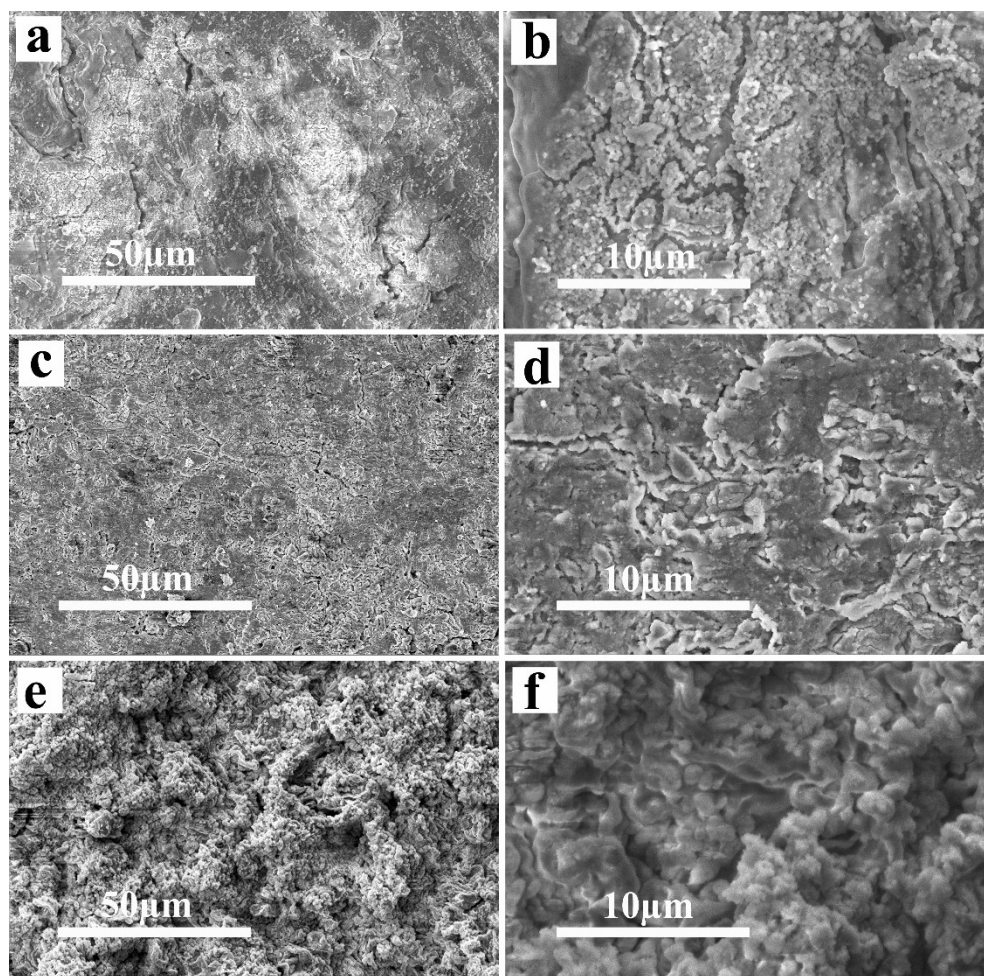


Figure S12. SEM images of the Li anodes in (a, b) PEGDME-10, (c, d) PEGDME-1 and (e, f) PEGDME-0 SPEs after 1000 h under a current density of 0.2 mA cm^{-2} .

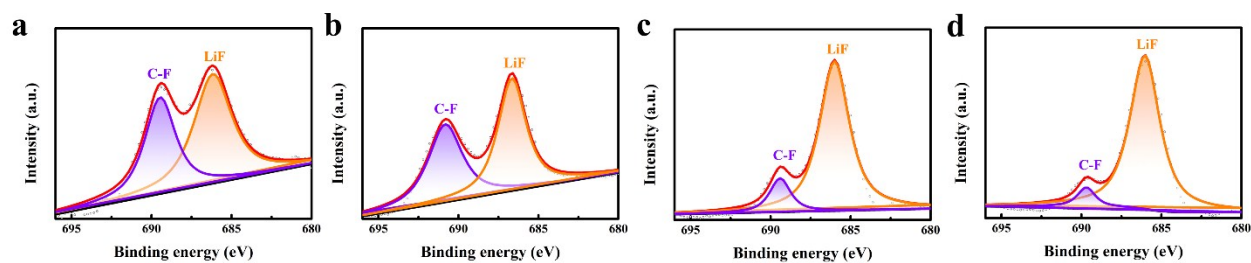


Figure S13. XPS results of Li after 50 h of plating and stripping in (a) PEGDME-10, (b) PEGDME-4, (c) PEGDME-1 and (d) PEGDME-0 SPEs.

To elucidate the mechanism for the improvement in electrochemical performance achieved by introducing the LiFSI salt into the PEGDME polymer, the Li-Li symmetrical cells using PEGDME-x SPEs operated at 0.2 mA cm^{-2} for 50 h were disassembled. The morphology of the Li anode and SEI components was examined by scanning electron microscopy (SEM) and X-ray photoelectron spectroscopy (XPS). As shown in [Figure S11a-c](#), the surface of the Li anode in the cell using PEGDME-10 exhibits a network morphology attributed to non-uniform Li deposition due to the existence of reactive defects on the Li anode.⁶ After extended cycling, nonuniform Li deposition results in surface cracking and lithium anode pulverization ([Figure S12a-b](#)), leading to increased overpotential and eventual short-circuiting. Promisingly, a LiTFSI/LiFSI ratio of 4/1 (PEGDME-4) results in a flat Li anode surface morphology ([Figure 2e-g](#)), which is maintained for a long cycling time of over 1000 h ([Figure S17a-b](#)). Further increasing the LiFSI ratio causes the rough surface to return. Compared to PEGDME-4, the Li deposition process with PEGDME-1 and PEGDME-0 SPEs is uniform and the Li deposition size enlarged ([Figure S11d-i](#)), even to several micrometers ([Figure S11g-i](#)). The raised Li deposition size and relatively uniform Li deposition process, in principle, are profitable for suppressing Li dendrite growth. Nevertheless, due to the large overpotential and large bias voltage applied on the PEGDME-0 SPE-based Li-Li symmetric cells, and the rugged surface is formed after long-term cycling, resulting in the occurrence of short-circuiting ([Figure S12e-f](#)). Compared to the single salt-based SPEs using either LiTFSI or LiFSI, the dual-salt SPEs (PEGDME-1 and PEGDME-4) maintain a relatively flat anode surface after extended cycling ([Figure S12c-d](#) and [Figure S17a-b](#)). The flat anode surface morphology with the dual-salt based SPEs aligns with the better electrochemical performance of Li-Li symmetric cells.⁷ It is well known that solid-electrolyte interface (SEI) influences Li plating/stripping behavior. Hence, XPS was used to examine the SEI of Li anodes paired with different SPEs. The results are

shown in Figure S13. The LiF ratio is observed to increase sharply with the increasing LiFSI ratio. It seems therefore that the LiFSI promotes the formation of a LiF-rich SEI on the Li surface, which in turn leads to uniform Li deposition.^{8,9}

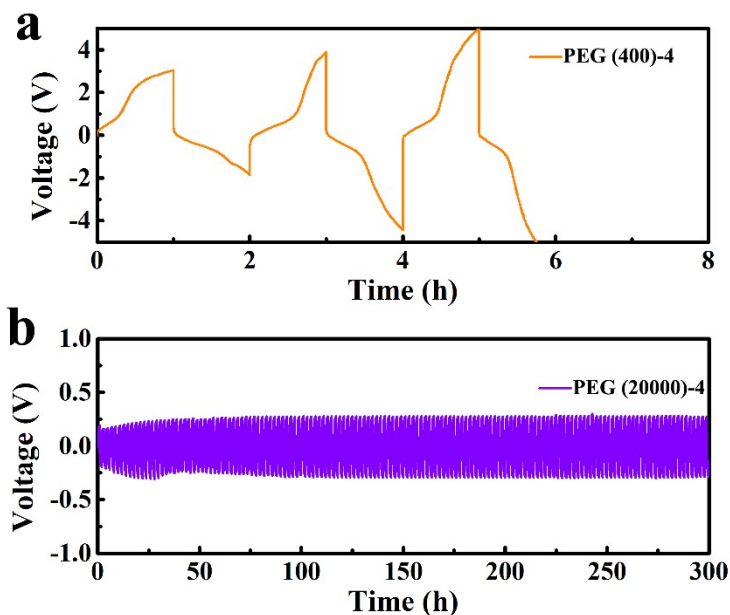


Figure S14. Cycling performance of Li-Li symmetrical cells with (a) PEG (400)-4 and (b) PEG (20000)-4 SPEs under a current density of 0.2 mA cm^{-2} (capacity: 0.2 mAh cm^{-2}).

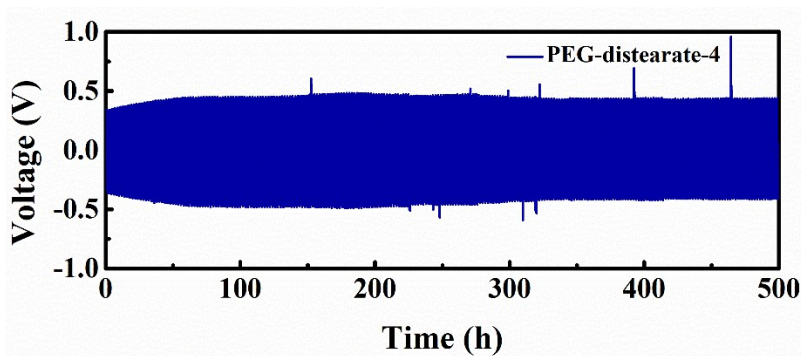


Figure S15. Cycling performance of Li-Li symmetrical cells with PEG-distearate-4 SPE under a current density of 0.2 mA cm^{-2} (capacity: 0.2 mAh cm^{-2}).

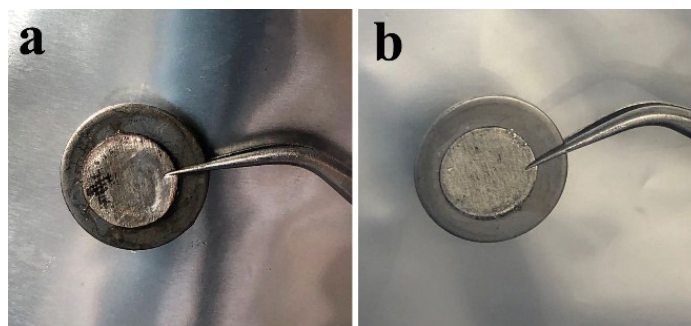


Figure S16. Optical images of (a) PEG-4 and (b) PEGDME-4 SPEs after 50 h of Li plating/stripping with a current density of 0.2 mA cm^{-2} .

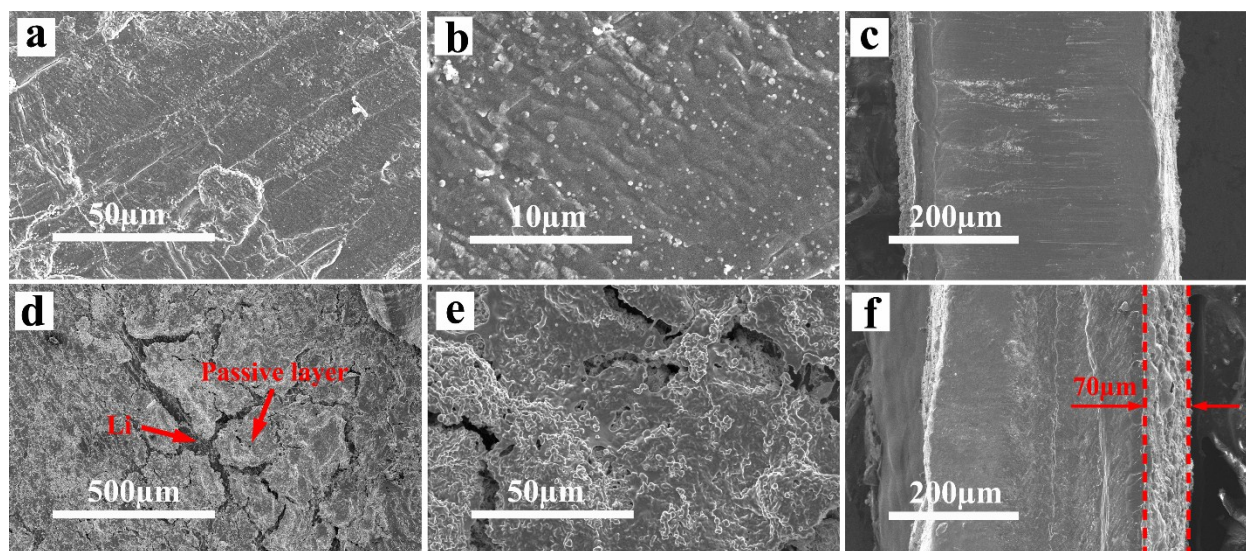


Figure S17. (a-b) Surface and (c) cross-section morphology of a Li anode in PEGDME-4 SPE after 1000 h. (d-e) Surface and (f) cross-section morphology of a Li anode in PEG-4 SPE after 300 h.

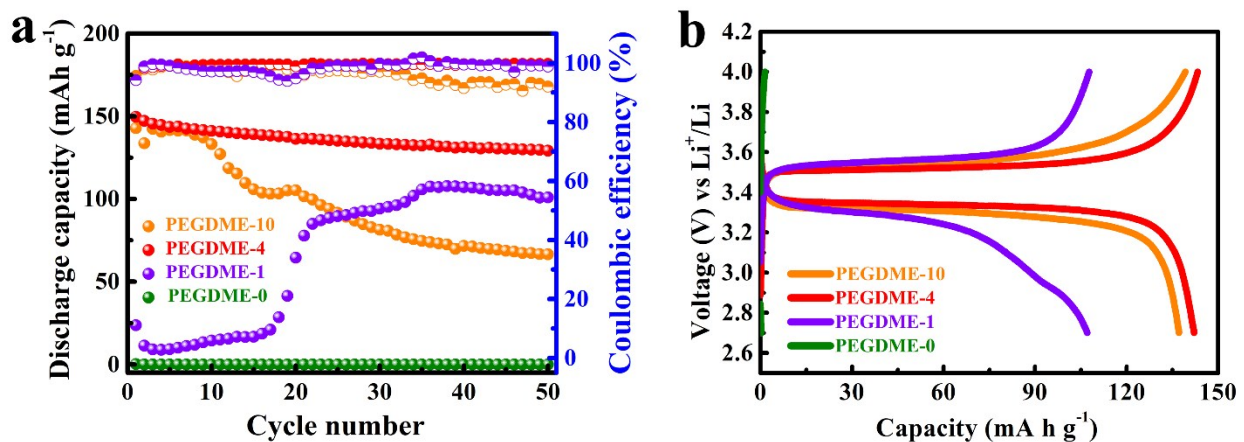


Figure S18. (a) Cycling performance and (b) charge/discharge profiles of Li-LFP coin cells using PEGDME-x SPEs at 0.1C (LFP loading: 6-7 mg cm⁻²).

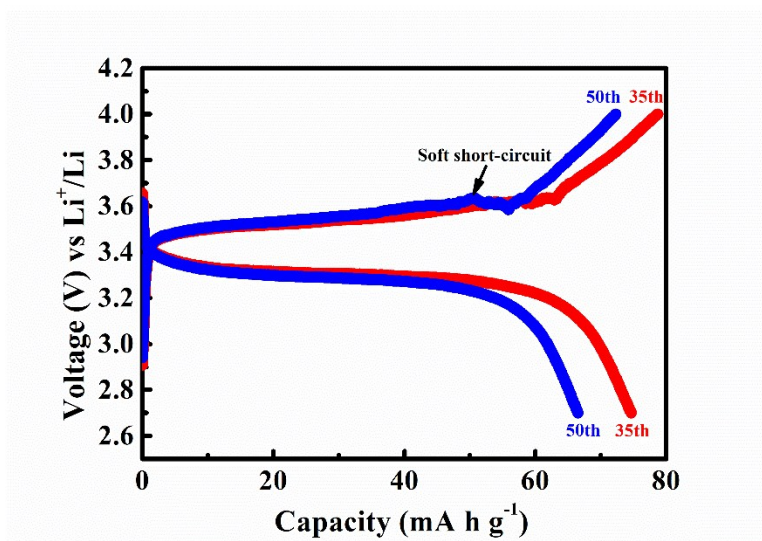


Figure S19. Charge/discharge profiles of Li-LFP coin cells using PEGDME-10 SPE for the 35th and 50th cycles (LFP loading: 6-7 mg cm⁻²).

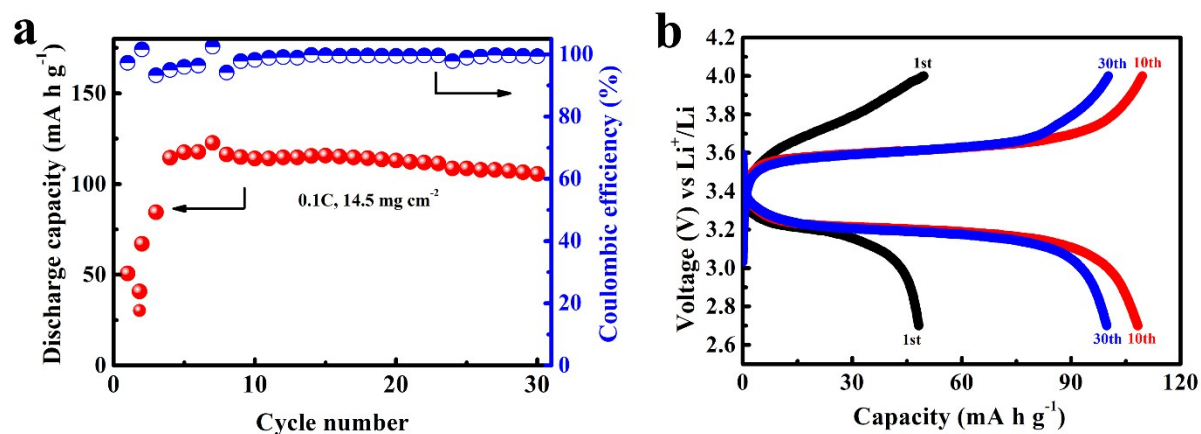


Figure S20. (a) Cycling performance of Li-LFP coin cells using PEGDME-4 SPE at 0.1C (LFP loading: 14.5 mg cm⁻²).

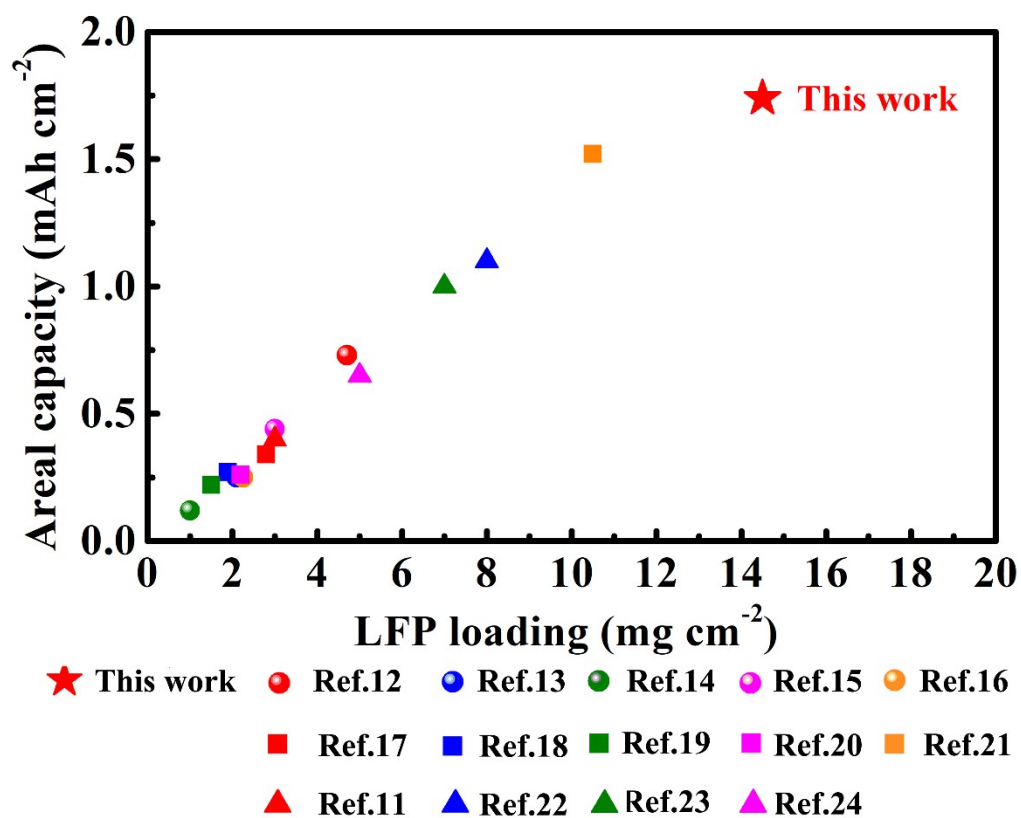


Figure S21. Comparison of the LFP loading and areal capacity of this work to that of recent publications.

The cycling stability of Li-LFP ASSLB coin cells assembled with PEGDME-x SPEs and LFP loadings of 6-7 mg cm⁻² is first evaluated at a galvanostatic charge/discharge C-rate of 0.1 C. As shown in [Figure S18](#), the low ionic conductivity of the PEGDME-0 SPE results in poor Li⁺ transport, large overpotential and no capacity output. Compared to PEGDME-0, the Li-LFP cell using PEGDME-1 exhibits an obvious activation process before reaching a steady-state after 20 cycles. This activation period can be attributed to the wetting process. Ultimately, a stable and reversible capacity of around 110 mAh g⁻¹ is achieved. Of the four SPEs, PEGDME-10 and PEGDME-4 show the highest ionic conductivity, leading to higher initial capacities of over 145 mAh g⁻¹. After 50 cycles, the Li-LFP cell using PEGDME-4 maintains a capacity of 130 mAh g⁻¹ and a Coulombic efficiency (CE) of around 100%, corresponding to a capacity retention of roughly 90%. In contrast, the capacity of the cell using PEGDME-10 drops sharply after 10 cycles. After 50 cycles, only a capacity of 66 mAh g⁻¹ remains. The quickly decaying capacity can be attributed to Li dendrite growth and dead Li formation in the presence of the single LiTFSI salt. This is further confirmed by the CE drop (from the 35th cycle) and shorted charging profiles in [Figure S19](#).^{10, 11} The Li-LFP coin cell results agree with the Li-Li symmetric cell results that the PEGDME-4 with dual-salts is the optimal SPE. It is well known that high loading cathodes and high areal capacities are critical to ensure high-energy-density cells for practical applications. A Li-LFP coin cell assembled with a higher LFP loading of 14.5 mg cm⁻² is therefore evaluated. As shown in [Figure S20](#), the cell demonstrates good cycling stability with a reversible capacity of around 120 mAh g⁻¹ for 30 cycles. This corresponds to an areal capacity of 1.74 mAh cm⁻², which is among the highest values in the SPE-based ASSLBs listed in [Figure S21](#) and [Table S1](#).

Table. S1 Summary of LFP with SPE performance reported in literature. (PEO: Polyethylene oxide; GF: glass fiber; LiTFSI: lithium bis(trifluoromethylsulphonyl)imide; SPE: Solid polymer electrolyte; LATP: $\text{Li}_{1.3}\text{Al}_{0.3}\text{Ti}_{1.7}(\text{PO}_4)_3$; LAGP: $\text{Li}_{1.3}\text{Al}_{0.3}\text{Ge}_{1.7}(\text{PO}_4)_3$; PLL: PEO-LiTFSI-LLZTO; CPE10: composite polymer electrolyte with 10% TiO_2 . CDQs: carbon quantum dots; DS-SPE: dual-salt solid polymer electrolyte; MUSiO₂: monodispersed ultrafine SiO_2 ; HSE: Hybrid solid electrolyte; PCL: Poly(ϵ -caprolactone); SN: Succinonitrile; LINTFSI: $\text{Li}[(\text{CF}_3\text{SO}_2)(\text{n-C}_4\text{F}_9\text{SO}_2)\text{-N}]$; PolyDOL:Poly (1,3-Dioxolane);)

Electrolyte	LFP loading (mg cm ⁻²)	Current density (mA cm ⁻²)	Areal capacity (mAh cm ⁻²)
PEGDME-4 (this work★)	14.5	0.25	1.74
PLL ¹²	4.7	0.08	0.73
PWO-CDQs ¹³	2.1	1.43	0.25
PEO-MUSiO ₂ ¹⁴	1.0	0.17	0.12
PEO-50%LATP ¹⁵	3.0	0.51	0.44
BN-PEO ¹⁶	2-2.5	0.68-0.85	0.22-0.28
DS-SPE ¹⁷	2.8	0.10	0.34
PCL/SN-SPE ¹⁸	1.9	0.06	0.27
LiTNFSI/PEO ¹⁹	1.5	0.03	0.22
HSE ²⁰	2.2	0.2	0.26
PEO@GF ²¹	10.5	0.18	1.52
PEO-Cs ⁺¹¹	3.0	0.26	0.4
LAGP70-SN9 ²²	8.0	0.27	1.10
PEO-LLZO ²³	7.0	0.12	1.00
PolyDOL ²⁴	5.0	0.17	0.63

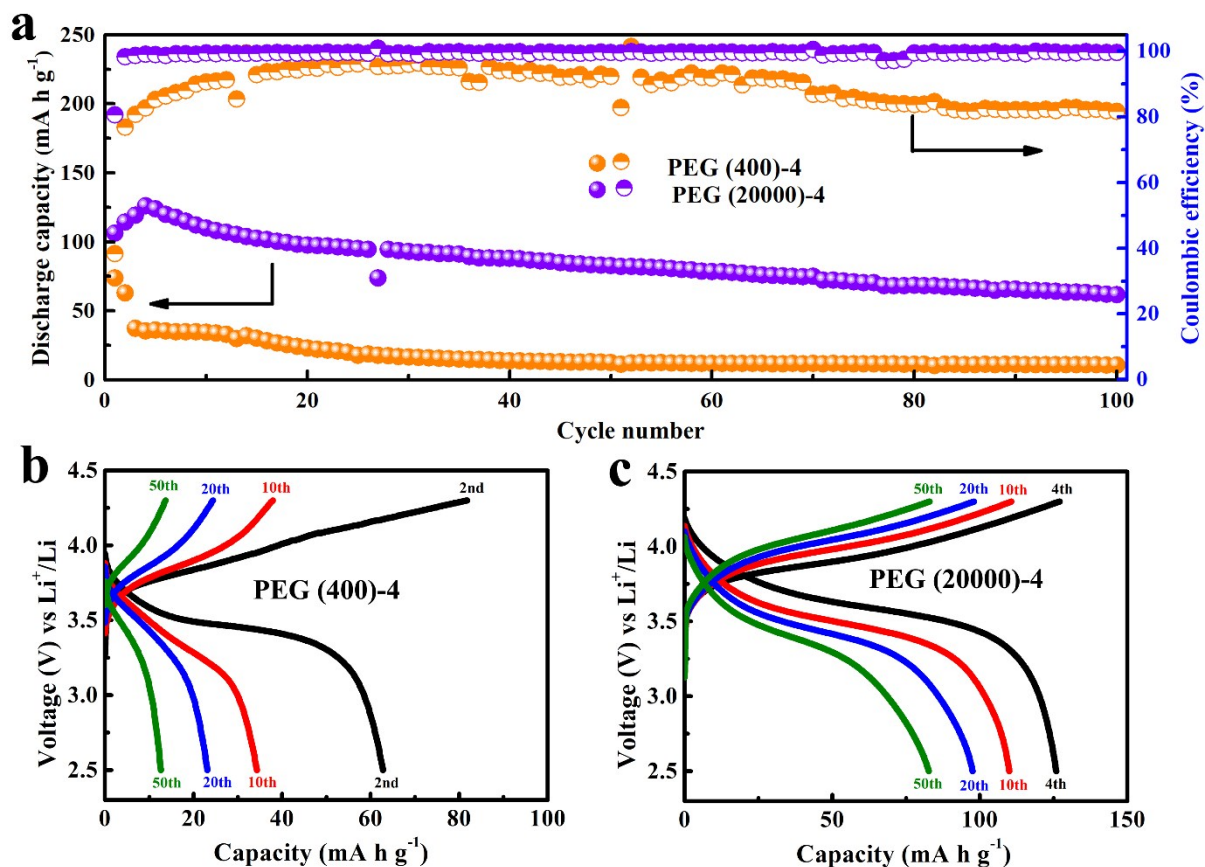


Figure S22. (a) Cycling performance and (b-c) relative charge-discharge profiles of Li-NMC532 coin cells using PEG (400)-4 and PEG (20000)-4 SPEs with an operating voltage range of 2.5-4.3 V at 0.2C.

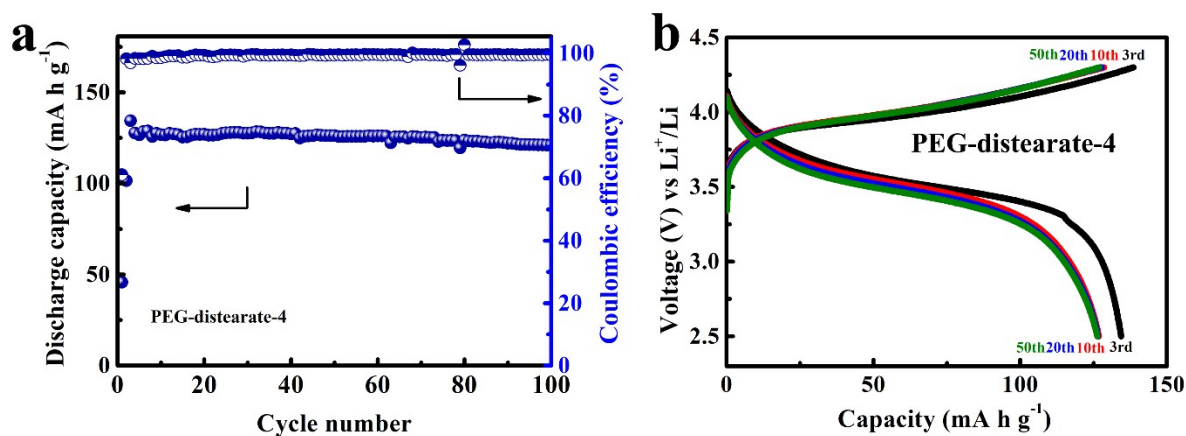


Figure S23. (a) Cycling performance and (b) relative charge-discharge profiles of Li-NMC532 coin cells using PEG-distearate-4 SPE with an operating voltage range of 2.5-4.3 V at 0.2C.

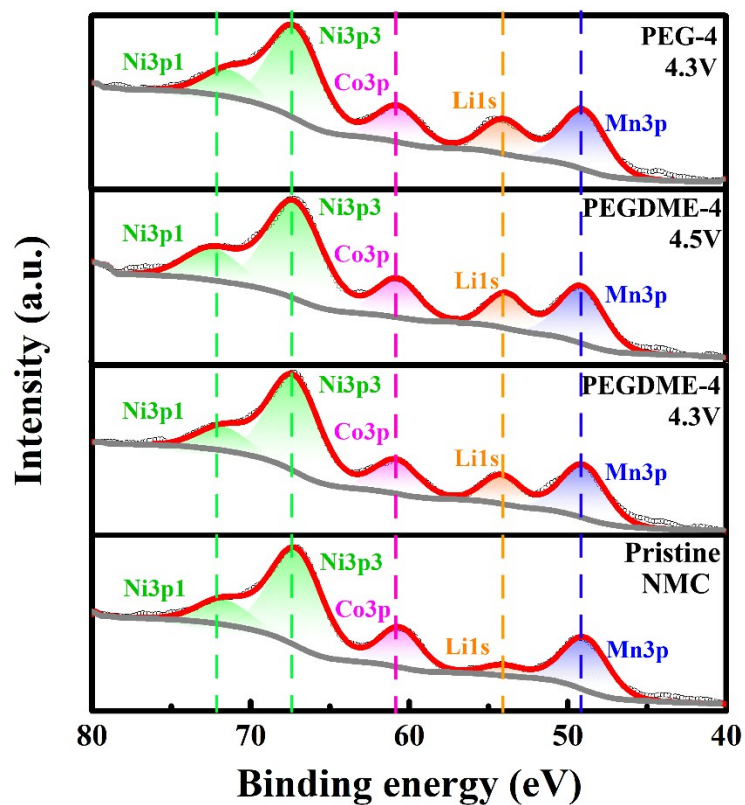


Figure S24. The XPS results (including Ni3p1, Ni3p3, Co3p, Mn3p and Li1s) of the NMC532 cathodes using different SPEs operating at different voltages.

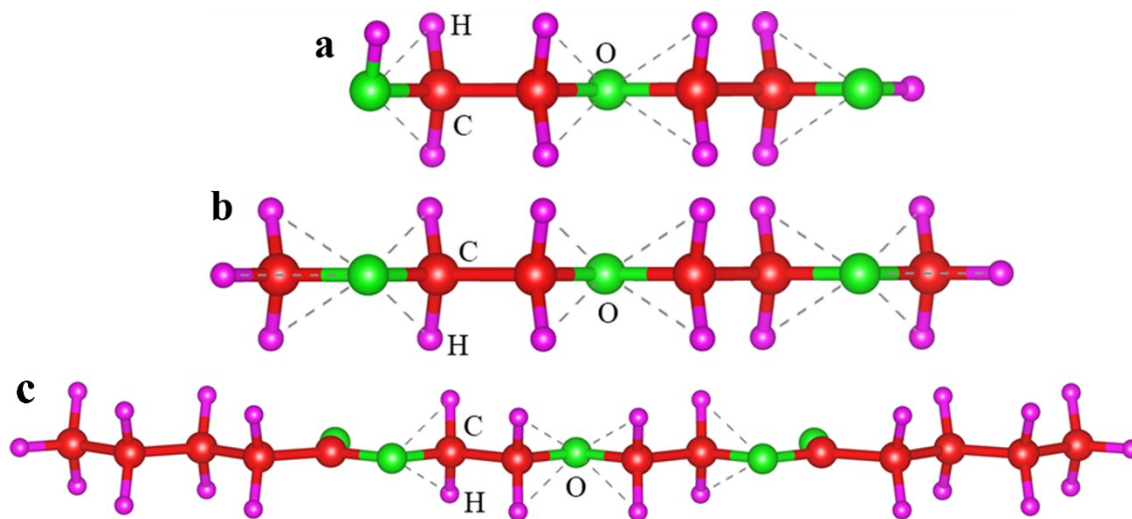


Figure S25. Molecular models of (a) PEG, (b) PEGDME and (c) PEG-distearate for DFT calculations.

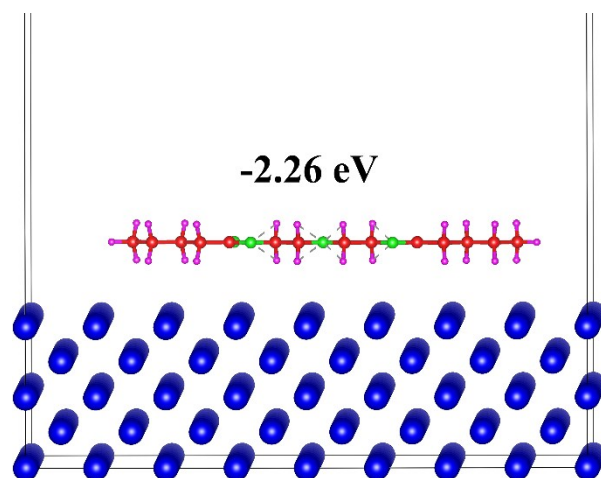


Figure S26. Parallel adsorption site on Li (100) surface for PEG-distearate molecule.

The lattice constant of Li was calculated to be 3.43 Å, which is in good agreement with previous theoretical results of 3.44 Å²⁵ and only slightly different from the experimental value of 3.49 Å.²⁶ As shown in [Table S2](#), the surface energy of (100) orientation (2.75 eV) is much lower than that of the (110) and (111) planes (3.06 eV and 3.49 eV), indicating that the (100) plane is the most stable surface. This trend is generally in accordance with the previous theoretical results on Li-metal surfaces.²⁵ Hence, in this work, only the (100) surface has been considered for the absorption energy calculations. For PEG-distearate molecule model construction, it is very hard to calculate a polymer molecule with such a big terminal group as $-\text{OCO}(\text{CH}_2)_{16}\text{CH}_3$, so we simplify the molecule with a similar terminal group $-\text{OCO}(\text{CH}_2)_3\text{CH}_3$ instead during calculation ([Figure S25](#)).

Table S2. The surface energies (eV/nm²) of Li slab surfaces.

	Our Cal.	Other Cal.		Exp.
(100)	2.75	2.68 ²⁵	2.92 ²⁷	-
(110)	3.06	2.97 ²⁵	3.22 ²⁷	3.26 ²⁸
(111)	3.49	3.41 ²⁵	3.61 ²⁷	-

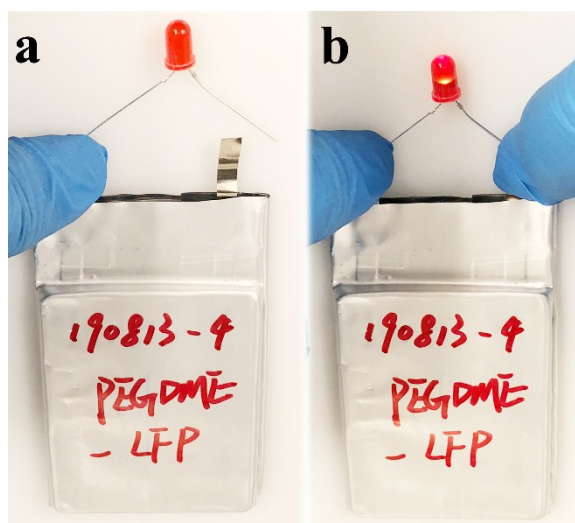


Figure S27. The optical images show a red LED light (a) before and (b) after being lit by a PEGDME-4 SPE-based ASSLB pouch cell.

References

1. J. P. Perdew, K. Burke and M. Ernzerhof, *Phys. Rev. Lett.*, 1996, **77**, 3865-3868.
2. K. Momma and F. Izumi, *J. Appl. Crystallogr.*, 2008, **41**, 653-658.
3. W. Reckien, F. Janetzko, M. F. Peintinger and T. Bredow, *J. Comput. Chem.*, 2012, **33**, 2023-2031.
4. J. B. Davis, F. Baletto and R. L. Johnston, *J. Phys. Chem. A*, 2015, **119**, 9703-9709.
5. Y. Xiang, M. Jiang, H. Xiao, K. Xing, X. Peng, S. Zhang and D.-C. Qi, *Appl. Surf. Sci.*, 2019, **496**, 143604.
6. C. Wei, H. Fei, Y. An, Y. Tao, J. Feng and Y. Qian, *J. Mater. Chem. A*, 2019, **7**, 18861-18870.
7. J. J. Hu, G. K. Long, S. Liu, G. R. Li and X. P. Gao, *Chem. Commun.*, 2014, **50**, 14647-14650.
8. G. G. Eshetu, X. Judez, C. Li, M. Martinez-Ibanez, I. Gracia, O. Bondarchuk, J. Carrasco, L. M. Rodriguez-Martinez, H. Zhang and M. Armand, *J. Am. Chem. Soc.*, 2018, **140**, 9921-9933.
9. G. G. Eshetu, X. Judez, C. Li, O. Bondarchuk, L. M. Rodriguez-Martinez, H. Zhang and M. Armand, *Angew. Chem. Int. Ed.*, 2017, **56**, 15368-15372.
10. Y. Lin, Y. Cheng, J. Li, J. D. Miller, J. Liu and X. Wang, *RSC Adv.*, 2017, **7**, 24856-24863.
11. X. Yang, Q. Sun, C. Zhao, X. Gao, K. Adair, Y. Zhao, J. Luo, X. Lin, J. Liang, H. Huang, L. Zhang, S. Lu, R. Li and X. Sun, *Energy Storage Mater.*, 2019, **22**, 194-199.
12. C. Z. Zhao, X. Q. Zhang, X. B. Cheng, R. Zhang, R. Xu, P. Y. Chen, H. J. Peng, J. Q. Huang and Q. Zhang, *Proc. Natl. Acad. Sci. U. S. A.*, 2017, **114**, 11069-11074.
13. C. Ma, K. Dai, H. Hou, X. Ji, L. Chen, D. G. Ivey and W. Wei, *Adv. Sci.*, 2018, **5**, 1700996.
14. D. Lin, W. Liu, Y. Liu, H. R. Lee, P. C. Hsu, K. Liu and Y. Cui, *Nano Lett.*, 2016, **16**, 459-465.
15. X. Ban, W. Zhang, N. Chen and C. Sun, *J. Phys. Chem. C*, 2018, **122**, 9852-9858.
16. B. Shen, T. W. Zhang, Y. C. Yin, Z. X. Zhu, L. L. Lu, C. Ma, F. Zhou and H. B. Yao, *Chem. Commun.*, 2019, **55**, 7703-7706.
17. S. Li, Y.-M. Chen, W. Liang, Y. Shao, K. Liu, Z. Nikolov and Y. Zhu, *Joule*, 2018, **2**, 1838-1856.
18. D. Zhang, L. Zhang, K. Yang, H. Wang, C. Yu, D. Xu, B. Xu and L. M. Wang, *ACS Appl. Mater. Interfaces*, 2017, **9**, 36886-36896.
19. Q. Ma, X. Qi, B. Tong, Y. Zheng, W. Feng, J. Nie, Y. S. Hu, H. Li, X. Huang, L. Chen and Z. Zhou, *ACS Appl. Mater. Interfaces*, 2016, **8**, 29705-29712.
20. W. Zhang, J. Nie, F. Li, Z. L. Wang and C. Sun, *Nano Energy*, 2018, **45**, 413-419.
21. X. Yang, Q. Sun, C. Zhao, X. Gao, K. R. Adair, Y. Liu, J. Luo, X. Lin, J. Liang, H. Huang, L. Zhang, R. Yang, S. Lu, R. Li and X. Sun, *Nano Energy*, 2019, **61**, 567-575.
22. Y.-C. Jung, M.-S. Park, C.-H. Doh and D.-W. Kim, *Electrochim. Acta*, 2016, **218**, 271-277.
23. A. I. Pitillas Martinez, F. Aguesse, L. Otaegui, M. Schneider, A. Roters, A. Llordés and L. Buannic, *J. Phys. Chem. C*, 2019, **123**, 3270-3278.
24. Q. Zhao, X. Liu, S. Stalin, K. Khan and L. A. Archer, *Nat. Energy*, 2019, **4**, 365-373.
25. M. Ebadi, D. Brandell and C. M. Araujo, *J. Chem. Phys.*, 2016, **145**, 204701.

26. C. Kittel, *Introduction to Solid State Physics, 8th Edition, Wiley, New York, 2004.*
27. C. Fiolhais and L. M. Almeida, *Int. J. Quantum Chem.*, 2005, **101**, 645-650.
28. W. R. Tyson and W. A. Miller, *Surf. Sci.*, 1977, **62**, 267-276.